Historical surface mass balance from a frequency-modulated continuous-wave (FMCW) radar survey from Zhongshan station to Dome A

Jingxue Guo[1], Wangxiao Yang[2], Yinke Dou[2], Xueyuan Tang[1], Jamin S. Greenbaum[3] (iD), Ruofan Dou[2], Yao Pan[2], Yuzhong Zhang[2], Minghu Ding[4], Su Jiang[1], Guitao Shi[5], Xiangbin Cui[1] and Bo Sun[1]

[1]Polar Research Institute of China, Shanghai 200136, China; [2]College of Electrical and Power Engineering, Taiyuan University of Technology, Taiyuan 030024, China; [3]Institute for Geophysics, University of Texas at Austin, Austin, TX 78758, USA; [4]State Key Laboratory on Severe Weather, Chinese Academy of Meteorological Sciences, Beijing 100081, China and [5]Key Laboratory of Geographic Information Science (Ministry of Education), School of Geographic Sciences and State Key Lab of Estuarine and Coastal Research, East China Normal University, Shanghai 200241, China

Abstract

Using frequency-modulated continuous wave radar data from the 32nd Chinese Antarctic Research Expedition in 2015/16, subsurface profiles were obtained along an East Antarctic inland traverse from Zhongshan station to Dome A, and four distinct regions were selected to analyze the spatiotemporal variability in historical surface mass balance (SMB). Based on depth, density, and age data from ice cores along the traverse, the radar data were calibrated to yield average SMB data. The zone 49–195 km from the coast has the highest SMB (235 kg m^{-2} a^{-1}). The 780–892 km zone was most affected by the Medieval Warm Period and the Little Ice Age, and the SMB during AD 1454–1836 (71 kg m^{-2} a^{-1}) was only one-quarter of that in the 20th century. The SMB in the 1080–1157 km zone fluctuates the most, possibly due to erosion or irregular deposition of snow by katabatic winds in low SMB areas with surface elevation fluctuations. Dome A (1157–1236 km) has the lowest SMB (29 kg m^{-2} a^{-1}) and did not decrease during Little Ice Age. Understanding the spatiotemporal variability of SMB in a larger space can help us understand the complex climate history of Antarctica.

1. Introduction

The Antarctic ice sheet is the largest volume of solid water on Earth, and the melting of this ice sheet under a warming climate will cause a significant increase in the global sea level (Tang and others, 2009; Rignot and others, 2011). The mass input on the surface of the Antarctic and Greenland ice sheets can be expressed by surface mass balance (SMB), which is the most important parameter when studying the state of ice sheets under different climatic conditions (Verfaillie and others, 2012; Lenaerts and others, 2019). SMB is influenced by slope, elevation, wind direction, wind speed and air temperature (Lenaerts and others, 2019). Although the SMB gradually decreases with distance inland from the coast, the SMB varies over several spatial scales, ranging from a few meters to hundreds of kilometers (Ding and others, 2011).

Observations of SMB in Antarctica are mainly obtained through on-site measurements and can be used to interpolate remote-sensing data. There are a variety of methods available for on-site ground observations, such as stakes in farms and lines, snow pits, snow micro-pens and firn/ice cores (e.g. Eisen and others, 2008; Kameda and others, 2008; Ding and others, 2011; Shepherd and others, 2012; Proksch and others, 2015). However, these methods provide SMB data at a low spatial resolution. For example, the stake data resolution of Ding and others (2011) is 15 km, and the measurements span only 20–30 years. The shortness of the studied time periods cannot be used to directly understand the characteristics of Antarctic SMB changes over century timescales. Ground-penetrating radar (GPR) has the advantage of providing continuous measurements over the ice sheet over larger distances than stakes and ice cores. When combined with other measurements, GPR allows the estimation of past SMB rates (e.g. Verfaillie and others, 2012; Meur and others, 2018).

The Chinese National Antarctic Research Expedition (CHINARE) has conducted several traverses from Zhongshan station to Dome A, collecting repeat observations along this transect (Mayewski and others, 2005; Cui and others, 2017). For these regular surveys, CHINARE uses a radar with a central frequency of 179 MHz to measure the ice sheet, allowing the characterization of the subglacial topography along the traverse (Cui and others, 2010). However, the frequency used implies that the internal reflecting horizons (IRHs) within several hundred meters at the top of the shallow ice sheet cannot be resolved. Therefore, in the summer of 2015/16, CHINARE used a frequency-modulated continuous wave (FMCW) radar to survey the same transect.

The purpose of this study is to reconstruct the average SMB from Zhongshan station to Dome A over the past few hundred years using high-resolution FMCW radar data. We first described the radar acquisition and processing. Based on the different ice surface characteristics along the traverse route (e.g. slope, meteorology), four distinct regions of the transect were identified for SMB analysis (Fig. 1). We traced IRHs in each transect section, dated them using available age and density information from ice cores collected along the traverse route between AD 1998 and AD 2005, and quantified uncertainties based on the combined radar and ice core measurement, resulting in estimated SMB rates. Finally, we discuss the temporal and spatial variability in the SMB rate in these four distinct transect regions and compare them to independently observed and modeled SMB data.

2. Data

2.1. Radar

FMCW radar, as a remote-sensing technology, has previously proven to be useful in snow research (e.g. Marshall and Koh, 2008), such as for snow stratigraphy measurement (e.g. Ellerbruch and Boyne, 1980; Koh and others, 2010), identification of snow features (e.g. Koh and others, 1996; Yankielun and others, 2004; Marshall and others, 2007), avalanche study (e.g. Gubler and Hiller, 1984), drainage structure detection in ice (e.g. Arcone and Yankielun, 2000) and object detection in the snow (e.g. Yamaguchi and others, 1992). This radar architecture has a higher resolution than a conventional pulsed radar, but the measurement range is smaller, so these two radar types can be combined to exploit each system's advantages (Uribe and others, 2014).

FMCW radar data were obtained during the 32nd CHINARE traverse (15–30 December 2015). CHINARE traveled mostly along 77°E longitude from Zhongshan station to Dome A and passed by Taishan station. The radar's control unit was set in the cabin of a Pisten Bully 300, and the antennas were placed parallel to each other at the top of the left side of the cabin. Because a metal rod would interfere with the signal, two rigid bamboo poles were used to fix the antennas. Both the transmitter and the receiver antenna were eight-element Vivaldi antenna arrays, which significantly narrowed the beamwidth. The half-power beamwidth of the antenna array was ∼15° in the E-plane (across track) and ∼60° in the H-plane (along track). Therefore, the antennas were installed 1.5 m from the vehicle on a nonmetal frame and 2 m above the ice surface, and the radar echo from the vehicle can be ignored. The vehicle moved at a constant speed of 14 km h^{-1}, and the transmitter and receiver operated continuously. A GPS antenna was mounted on the roof for geolocation and moved at the same speed.

In this radar system, the transmitting antenna produces an electromagnetic wave with a frequency of 0.5–2 GHz and a variation period of 4 ms, and the wavefront propagates downward. As the depth increases, the intensity of the reflected signal changes due to variations in the complex dielectric permittivity with increasing depth. The real part of the complex dielectric permittivity is mainly affected by density changes, whereas the imaginary part is mainly affected by electrical conductivity and dielectric anisotropy (Kovacs and others, 1995; Eisen and others, 2008). For our FMCW radar data, density, which increases with depth in the firn column until it stabilizes near 830 kg m^{-3} (Eisen and others, 2008), has the strongest influence on the complex dielectric constant (Kanagaratnam and others, 2001). We analyze the density characteristics in more detail in Section 3.1.

The variations in the complex dielectric permittivity with depth are laterally consistent, which creates continuous reflections called IRHs (Verfaillie and others, 2012). A radar echogram typically shows multiple IRHs stacked vertically, presenting a clear layered structure. IRHs from our traverse shown in Figure 2a are spatially continuous, and the formation time of a layer is considered isochronous (Eisen and others, 2008). Due to the influences of the surface slope, elevation, wind direction, wind speed and other factors, SMB variability will impact the depth of the same IRH along the transect (highlighted for three IRHs in Fig. 2b). Therefore, SMB can be reconstructed from IRH depths. The average thickness of the ice sheet from Zhongshan station to Dome A is 2037 m (Cui and others, 2010), while the FMCW radar only provides IRH within ∼100 m from the surface, so finite strain can be ignored (Waddington and others, 2007), and the SMB can be calculated directly from the age and depth of the IRH and the density of the ice core.

The radar profiles collected between Zhongshan station and Dome A (with a total length of 1236 km) were processed. In practice, when tracking an IRH over a range of more than 100 km, lateral discontinuities in the IRH are often found (Fig. 2), and it is difficult to trace a single IRH. In some locations, a complex structure in the ice sheet or a technical issue such as a break in the field recording can result in the loss of lateral continuity of the IRH. Figure 2c shows an example of a fold and discontinuity affecting multiple IRHs and Figure 2d displays strongly sloping IRHs. Such IRH geometries may be due to local ice flow causing overlap from different IRHs and snow mixing to cause radar reflection distortion (Arcone and Jacobel, 2010a, 2010b; Dahl-Jensen and others, 2013). Additionally, the melting of snow at the surface will also lead to the disappearance of IRH (e.g. Arcone and Jacobel, 2010b; Jacobel and Hodge, 1995).

Based on the characteristics of topography, SMB, IRH continuity, etc., four distinct transect regions (Fig. 1) were identified. Due to the limitation of radar detection depth and IRH discontinuity, IRHs in the same year cannot be extracted across these regions at the same time. Instead, three random ages of IRHs in each region were manually selected and tracked (e.g. Fig. 2b) and TWT was converted to depth (as described in Appendix A) for which we calculate the SMB over the past few hundred years. We define these four zones as follows:

Zone 1 is located 49–195 km from the coast, with steep and gradually decreasing slopes along the traverse (slopes range from 6.47 to 18.19 m km^{-1}).

Zone 2 is located 780–892 km from the coast, located downstream of the descending slope, and the aspect is flat, with a steady increase in slope along the traverse (average slope of 1.99 m km^{-1}).

Zone 3 is located 1080–1157 km from the coast, where the slope is not high (average slope of 1.97 m km^{-1}); this transect region is characterized by surface dunes ranging from tens to several kilometers in size (Ding and others, 2011).

Zone 4 is located in the Dome A area 1157–1236 km from the coast and the terrain is extremely flat with an average slope of 0.155 m km^{-1}.

2.2. Firn/ice cores

Four ice cores were retrieved along the traverse between AD 1998 and AD 2005, which are used to provide age and density constraints for the three IRHs in all four regions.

Ice core LGB69 is located in zone 1 and is from a site close to the coast with an annual SMB of 282 kg m^{-2} a^{-1} (Xiao and others, 2005). Li and others (2012) used the seasonal variation in several sea salt ions in the ice core to determine the age–depth relationship of LGB69. Due to the ambiguity of some seasonal cycles, the maximum error is ±2 years.
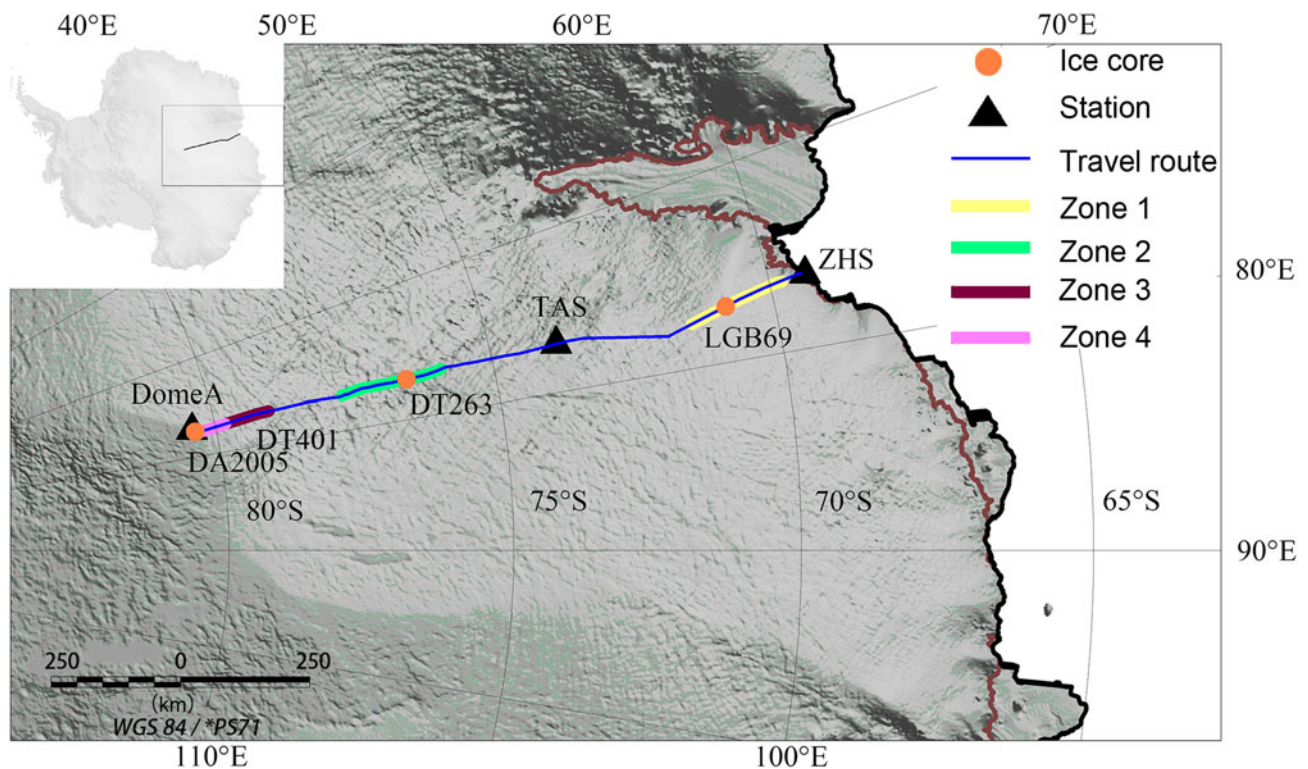
Fig. 1. Map of the radar traverse route from Zhongshan station to Dome A shown by a blue line. The four distinct transect regions discussed in this study (zone 1, 49–195 km; zone 2, 780–892 km; zone 3, 1080–1157 km; and zone 4, 1157–1236 km from the coast) are highlighted in yellow, green, dark red and magenta, respectively. Orange dots indicate the locations of the ice cores used in our study (LGB69, DT263, DT401 and DA2005), and black triangles indicate the Zhongshan (ZHS) station, Taishan (TAS) station and Dome A.

Ice core DT263 is located in zone 2. The area from which the ice core was extracted is close to the steep slope on the north side of Dome A, and the SMB is relatively low, so it is impossible to measure the age only based on Na^+ seasonal variation. Zhou and others (2006) used the concentration of nonsea salt SO_4^{2-} in the ice core to determine the age–depth relationship, and the error is ∼±5 years.

Ice core DT401 is located at the downstream end of zone 3. Ren and others (2010) also used the concentration of nonsea salt SO_4^{2-} to determine the age–depth relationship. The age error at the bottom of the ice core was estimated to be ±40 years.

Ice core DA2005 is located in zone 4 (Dome A region), which has one of the lowest SMBs in Antarctica (Hou and others, 2007). Jiang and others (2012) calculated the average SMB by using the volcanic record in the ice core. The error in the dating results is ±11 years (Table 1).

3. Methods

To obtain SMB from these radar IRHs, the following process is followed:

(1) Three IRHs are traced along each transect region and their TWT is measured.
(2) As radar returns are measured in TWT, the depths of the IRHs traced are obtained by dividing TWT by the speed of electromagnetic waves in ice calibrated by the density changes with depth measured at the colocated ice core sites (see Appendix A).
(3) The IRHs are matched to the dated volcanic record contained in the ice core, and the ages of the IRHs are assigned by interpolating the ages from the volcanic record.
(4) The average density between IRHs is obtained using an empirical formula (Cuffey and Paterson, 2010) and combined

with the ages of the IRHs allows the calculation of the average SMB between IRH pairs.

3.1. Density

Density affects the electromagnetic wave velocity in snow, which affects the IRH depth and SMB calculated from the IRHs (see Appendix A; Verfaillie and others, 2012). Because our study area traverses a large part of East Antarctica, it is necessary to consider the variability of densities among regions, and the ice core in each area is used to calibrate the depth–density relationship (Verfaillie and others, 2012; Meur and others, 2018). The densification process can be calculated according to the densification model from Cuffey and Paterson (2010) defined as

$$\rho(z) = \rho_i - (\rho_i - \rho_s) \exp(-Cz) \tag{1}$$

where ρ is the snow (firn) density at depth z; ρ_i is the pure ice density (i.e. 918 kg m^{-3}; Kanagaratnam and others, 2001); and ρ_s is the snow density at the surface. C is a constant, defined as $C = 1.9/z_t$, where z_t is the firn/ice transition depth (depth at the density of 830 kg m^{-3}). The surface snow density from Zhongshan station to Dome A is between 300 and 500 kg m^{-3}, and there is no clear functional relationship with coastal distance. The values of the average surface snow density ρ_s of each region are shown in Table 2. The estimated measurement accuracy is 95% (Ding and others, 2011). z_t is also variable along the transect. The general trend is that the transition depth is greater farther from the coast. Therefore, based on the actual measurement of the depth–density relationship in the four ice cores (LGB69, DT263, DA2005 and DT401), the transition depth corresponding to the critical density of 830 kg m^{-3} is determined with a fitting curve, as shown in Figure 3.
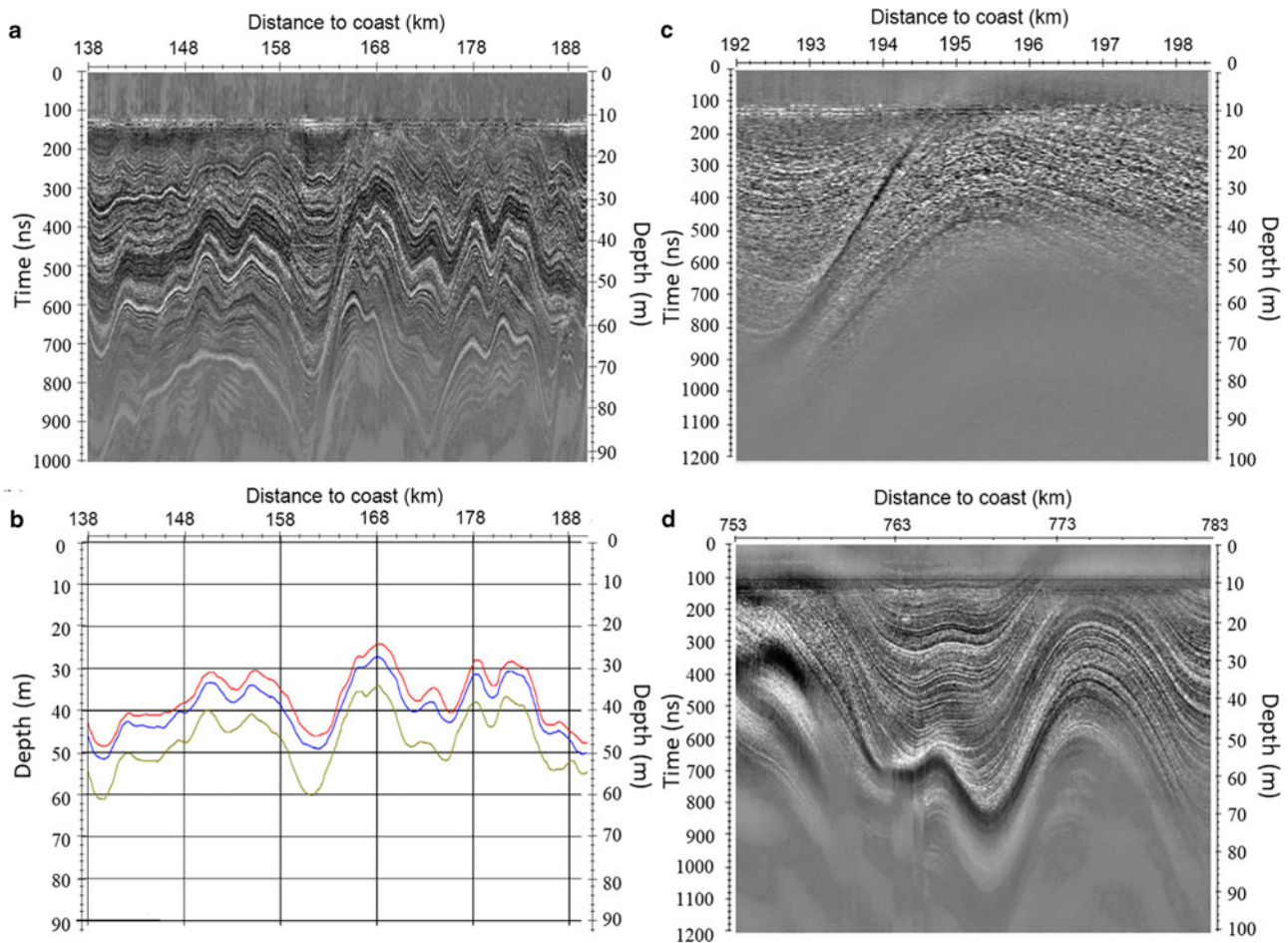
Fig. 2. FMCW radar profiles and interpretation. (a) Part of the radar profile and IRHs in zone 1 (138–191 km from the coast). (b) Three IRHs randomly extracted from (a). (c) IRH folds and discontinuities at the end of zone 1 (192–199 km from the coast). (d) Concave and convex patterns in the IRHs at the end of zone 2 (753–783 km from the coast).

Table 1. Location, depth, elevation, drill date, std dev. of the year (year std dev.), mean surface air temperature, record length, time span, references and accumulated depth during the period from drilling the ice core to radar observation (Acc dep.) for the selected ice cores

Ice core	Latitude °S	Longitude °E	Depth m	Elevation m a.s.l.	Drill date AD	Year std dev. %	Mean surface air temperature °C	Record length years	Time span	Acc dep. m	References
LGB69	70°50'07"	77°04'29"	101.5	1854	2002	0.68%	−27.2	294	AD 1708–2001	5.02	Li and others (2012)
DT263	76°32'28"	77°01'32"	82.5	2800	1998	0.64%	−43.0	780	AD 1215–1996	2.39	Zhou and others (2006)
DT401	79°01'00"	77°00'00"	102.65	3760	1999	1.5%	−54.3	2682	BC 682–AD 1999	1.67	Ren and others (2010)
DA2005	80°22'00"	77°22'00"	109.9	4092.5	2005	0.38%	−58.5	2840	BC 840–AD 1998	1.16	Jiang and others (2012)

Table 2. Firn/ice transition depth (z_t), average SMB, average surface snow density (ρ_s), and correlation between density model and observed densities in ice cores for each transect zone

Zone	Firn/ice transition depth m	Average SMB[a] kg m^{-2} a^{-1}	Average surface snow density[b] kg m^{-3}	Correlation
Zone 1	74.5	157	403	0.990
Zone 2	87.0	53	380	0.972
Zone 3	62.1[b]	75	390	0.968
Zone 4	96.5	35	320	0.992

[a]Results from Ding and others (2011).
[b]Results from Qin and others (2000).

Figure 3 was constructed by regionally selecting the parameters of Eqn (1) and comparing them to the measurements of the ice core, and the results show a high (>0.968) correlation (Table 2).

The maximum error between the observed and modeled density is 29 kg m^{-3}.

When snow density is higher than ~550 kg m^{-3}, the densification rate gradually decreases (Herron and others, 1980). Therefore, for IRHs, it is located below the depth corresponding to this critical density (~20 m depth), the impact of the densification process and the error in estimating the age will be relatively small. In this study, the depths of the IRHs tracked in each of the regions were >20 m, which limited the impact of the densification process on SMB estimate uncertainties.

3.2. Volcanic eruption record

3.2.1 Calibration of the depth of the volcanic record
In addition to the ice core density, the calculation of SMB also requires the age of the IRH, which requires developing an age–
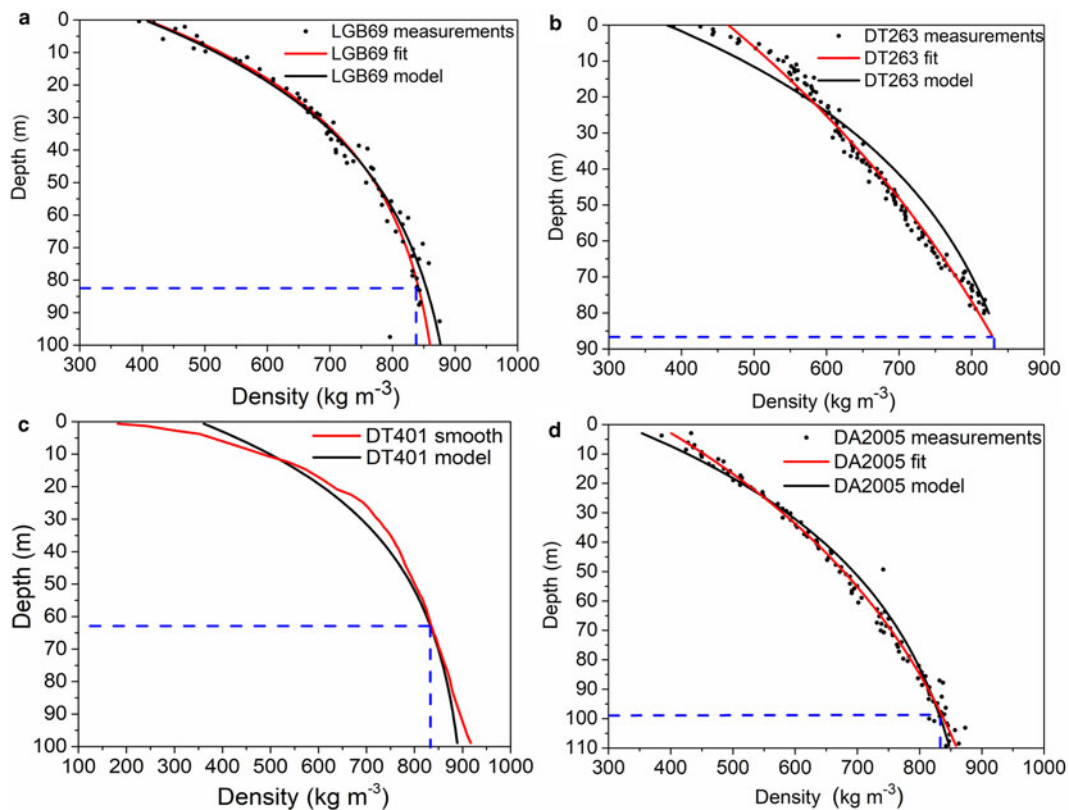
Fig. 3. Observed and modeled depth–density relationship for all four ice cores: (a) LGB69, (b) DT263, (c) DT401 and (d) DA2005. Black dots represent the ice core density measurements, and their fits or smooths (red line) are compared to the densification model (black line). Note that only the fitted data based on measurement data are given at (c) DT401 due to the lack of raw data. The firn/ice transition depth according to the critical density of 830 kg m^{-3} is indicated by a blue dashed line.

depth relationship for each ice core. The depth of IRH directly affects the result of SMB and needs to be calibrated. The radar data were collected in the 2015/16 season; thus, a time lag exists between when the ice cores were drilled and when the radar data were collected. During this time lag, additional snowfall caused an increase in the depth of previously identified volcanic layers. Due to the lack of continuous observations at the site, the average SMB has been used to invert for the increased snow thickness over the past few decades. Eqn (1) is used in the inversion process (Cuffey and Paterson, 2010), and the results are shown in Table 1.

3.2.2 Identification of volcanic eruption signals

Although the depth of the volcanic record was preliminarily calibrated in Section 3.2.1, there are still depth errors due to factors of diffuse scattering and densification process. Therefore, we used the characteristics of the volcano signal in the radar-gram for the secondary calibration of the depth. The Samalas volcano in Indonesia erupted in AD 1257, injecting sulfate aerosols into the stratosphere (Lavigne and others, 2013). Acid precipitation produced on the plateau of East Antarctica in AD 1260 (Delmas and others, 1992) is preserved in many ice cores, such as DT263, DT401 and DA2005, which all show similar volcanic signal profiles (Moore and others, 1991; Zhou and others, 2006; Ren and others, 2010; Jiang and others, 2012).

Zhou and others (2006) analyzed ice core DT263 and found four volcanic layers with a depth interval of ~1 m between records (Table 3). Four IRHs are clearly visible in the box in Figure 4a, which also exhibit similar distribution characteristics in the ice core. The same volcanic layer (volcanic layer D16 in Table 3) is also present in ice core DA2005, and the nonsea salt SO_4^{2-} in the ice core exhibits abnormal values (Jiang and others, 2012).

There are three additional IRHs around volcanic layer D16 with a depth interval of ~1 m between IRHs in the radar-gram in Figure 4b. Although the two regions span several hundred kilometers, the volcanic layers are present in both zones, which reinforce the isochronous characteristics of our traced IRHs.

This volcanic layer deposited in AD 1260 has wide coverage in East Antarctica and has obvious distribution characteristics that can be widely used for data calibration. As shown in Table 3, the std dev. of depth is within 2%.

3.3. Calculating SMB from the IRHs

The radar IRH depths were combined with the ice core age and density data to calculate SMB following the standard equation from Cuffey and Paterson (2010):

$$\text{SMB} = z\rho a^{-1} \tag{2}$$

where z represents the depth (m) of the IRH; ρ is the firn/snow density (kg m^{-3}) at the corresponding depth (since ρ is not uniform in the actual environment, the function $\rho(z)$ gradually increases with depth as defined in Eqn (1)); and a is the age (in years) of the layer. Since this formula is more suitable for SMB calculations within ~30 m, it is improved by integrating the density between IRHs (Meur and others, 2018). Eqn (2) thus becomes

$$\text{SMB} = \frac{\int_{z_{n-1}}^{z_n} \rho(z)\,\mathrm{d}z}{a_n - a_{n-1}} \tag{3}$$

Eqn (3) represents the average SMB from the year a_{n-1} to the year of a_n. In this equation, the depth z corresponds to the bounding

Table 3. Characteristic volcanic layers in ice cores DT263 and DA2005

Volcanic layer	Age AD	Depth at DT263[a] m	Depth at radar-gram m	Depth std dev. %	Depth at DT401[b] m	Depth at radar-gram m	Depth std dev. %	Depth at DA2005[c] m	Depth at radar-gram m	Depth std dev. %
D13	1286	74.793	76.018	1.23	37.98	38.48	1.31	–	–	–
D14	1277	75.656	76.810	1.15	–	–	–	–	–	–
D15	1269	76.469	77.646	1.18	–	–	–	–	–	–
D16	1260	77.623	78.218	0.60	39.63	40.40	1.94	35.5	36.21	2.0

[a]Results from the depth of the volcanic layers in Zhou and others (2006) and corrected radar observations.
[b]Results from Ren and others (2010).
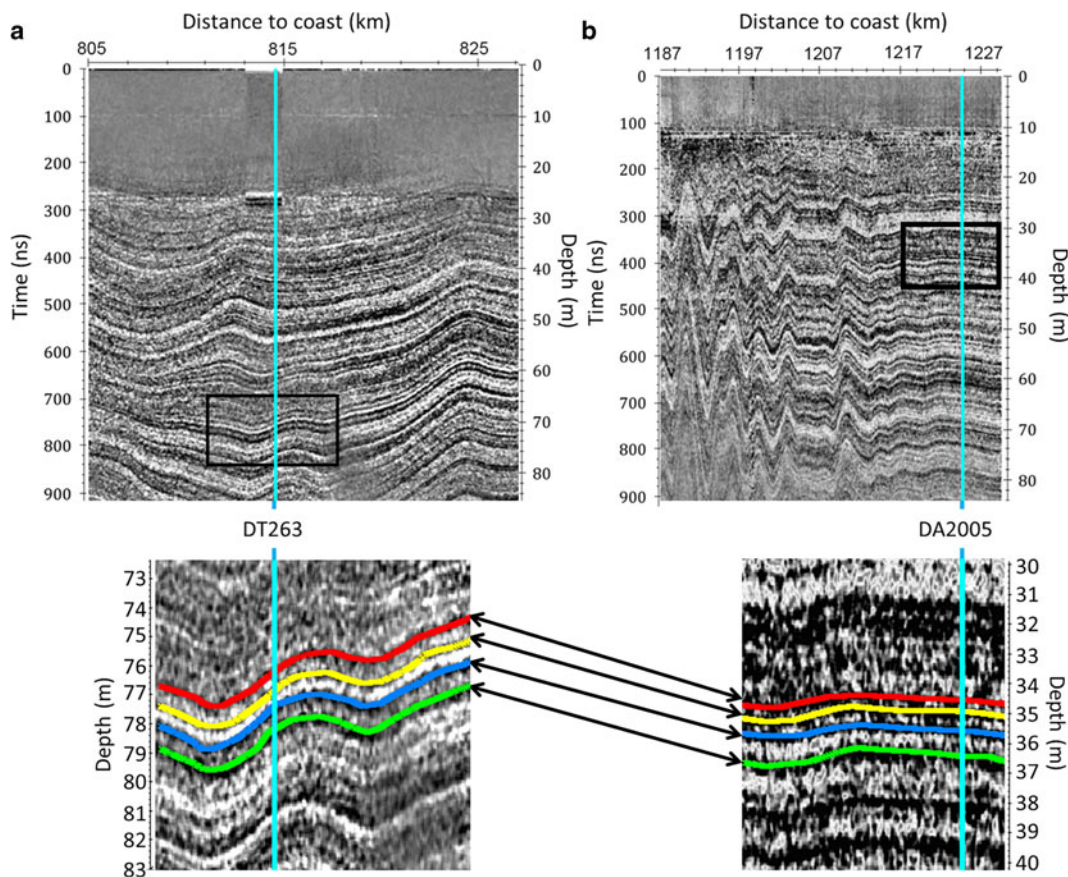[c]Results from Jiang and others (2012).

Fig. 4. The same four volcanic layers (D13–D16) are shown on partial radar-grams from zones 2 and 4. (a) Radar-gram of a transect within zone 4. Ice core DA2005 is located ~1225 km from the coast and is represented by a blue vertical line. Magnifying the area in the black box reveals four IRHs that are tracked manually (red, yellow, blue and green). (b) Radar-gram of a transect within zone 2, which crosses the location of ice core DT263. The bottom panel shows an enlarged version of the black box, in which the four IRHs are tracked, corresponding to the same IRHs in (a), as indicated by the black arrows.

IRH depths. For age-indeterminate layers, the age a is obtained by interpolation between the ages of volcanic layers.

3.4. Error estimates

Unlike stakes in farms, radar measurements are an indirect method of measuring the SMB. The radar processing applied, the assignment of the IRH depths and ages, and the chosen parameter values all affect the resulting SMB rates obtained. These various sources of uncertainty will lead to SMB uncertainty, which we decompose into the following components:

(1) The largest error is caused by the uncertainty in the density–depth relationship (δ_1, in Eqn (4)), which affects the SMB calculated according to Eqn (3). Although the use of regional parameters in Eqn (1) provides a high correlation between modeled and measured densities, density errors still exist with a maximum error of 29 kg m^{-3} at ice core DT263. This results in an SMB error of ~±3.0 kg m^{-2} a^{-1}.

(2) The high-frequency signals emitted by the FMCW radar can cause diffuse scattering, which increases the width of the IRHs in the radar profile and makes it difficult to track IRHs. In this study, tracking is performed manually, and the uncertainty in the IRH TWT caused by human error (δ_2, in Eqn (4)) is ~±2 ns. For an average wave velocity of 0.185 m ns^{-1} within ~100 m, the depth uncertainty is ±0.37 m, which results in an SMB error of ±0.32 kg m^{-2} a^{-1}.

(3) Dome A (zone 4) has one of the lowest SMBs in Antarctica. Hou and others (2007) estimated that the SMB of Dome A
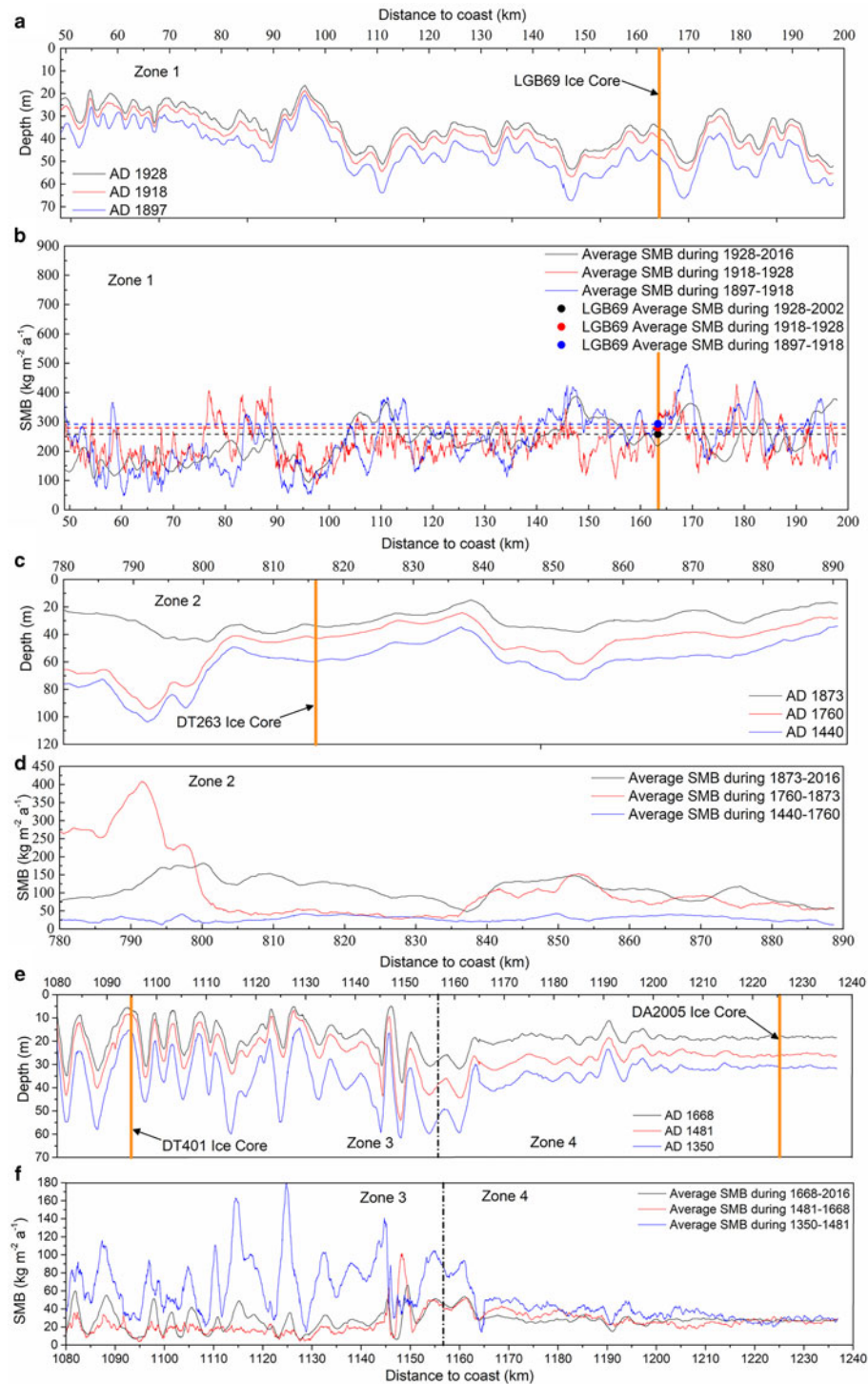
Fig. 5. The depths of the three IRHs and the corresponding SMB rates between pairs of IRHs in (a, b) zone 1, (c, d) zone 2 and (e, f) zones 3 and 4. Zones 3 and 4 are contiguous, so they are shown on the same panel. The ice cores used for calibration in each area are marked with yellow lines, and the average SMB data for ice core LGB69 are provided in (b). No such data are available for the other ice cores.

from AD 1966 to AD 2004 was ∼2.3 cm w.e. a^{-1}. The vertical resolution of the radar system is 6.16 cm, and considering diffuse scattering, the IRHs may contain multiple annual layers. The dating error due to the radar vertical resolution is ∼±3 years when resulting in an SMB error of 1.06 kg m^{-2} a^{-1} (δ_3, in Eqn (4)); this error is lower in high SMB regions.

(4) The average SMB in ice core DA2005 over a period of time is calculated in the form of w.e. Any fluctuations in the actual SMB during this period will deviate from the average rate, resulting in a certain error in determining the age–depth relationship of the ice core. Under the influence of the low SMB in Dome A, the uncertainty in the volcanic layer depth (δ_4, in Eqn (4)) will produce a large age error, and the maximum

value reaches 11 years (Jiang and others, 2012), which results in an average SMB error of 0.92 kg m^{-2} a^{-1}.

Assuming the above factors are uncorrelated, the maximum SMB error is calculated as follows:

$$\delta_{SMB} = \sqrt{\delta_1^2 + \delta_2^2 + \delta_3^2 + \delta_4^2} \qquad (4)$$

From Eqn (4), we obtain a maximum error of 3.56 kg m^{-2} a^{-1}, dominated by the error in the density. There are some differences in the process of densification between regions, and the error can be improved by retrieving additional ice core age and density measurements along the transect.

Table 4. Average IRH depth, age, std dev. of SMB and average SMB between the IRH and the one above it or ice surface in each transect region

Zone	Distance to coast km	Average IRH depth m	Age AD	Average SMB kg m^{-2} a^{-1}	Entire average SMB kg m^{-2} a^{-1}	Std dev. %
Zone 1	49–195	35.47	1928	235	235	20.6
		38.64	1918	226		
		45.31	1897	237		
Zone 2	780–892	30.01	1873	111	65	32.1
		47.48	1760	109		
		59.97	1440	29		
Zone 3	1080–1157	18.58	1668	28	35	38.7
		25.02	1481	23		
		37.83	1350	71		
Zone 4	1157–1236	18.38	1668	27	29	12.3
		26.36	1481	28		
		32.89	1350	35		

4. Results

We examine the SMB obtained from the GPR data in the four distinct regions. On average, the three IRHs interpreted in each region provide the temporal and spatial SMB variation, as shown in Figure 5 and Table 4. Overall, the SMB decreases with increasing proximity to Dome A.

Among the four transect regions, zone 1 is the nearest to the coast (Fig. 5a). The average SMB during AD 1897–2016 is 235 kg m^{-2} a^{-1}, with a std dev. of 20.6% across the zone (Fig. 5b). In agreement with the observations of Ding and others (2011), this is the area with the highest SMB. Mainly due to the steep slope and proximity to the coast, when water vapor is transported inland from the sea, most of the vapor is deposited as snow in the coastal region, resulting in a higher SMB in zone 1 than in the other areas (e.g. Fujita and others, 2011; Verfaillie and others, 2012).

According to the on-site investigation of Ding and others (2011), the surface aspect in zone 2 is flat, the average wind speed is 3.9 m s^{-1} (oriented northeast), and there are well-developed wind crusts and strong wind ablation (Ma and others, 2010). This causes highly variable snow accumulation at the spatial scales of ∼20 km, which is the main cause of the variability in the SMB (Frezzotti and others, 2002, 2005). The average SMB during AD 1440–2016 is 65 kg m^{-2} a^{-1}, with a std dev. of 32.1% across the zone (Figs 5c, d).

Zone 3 (Figs 5e, f) shows large fluctuations or even truncations in the IRHs in this region, and the accumulation profile accordingly shows large fluctuations over small distances. However, in zone 4, the three IRHs are relatively flat, which is consistent with the terrain in the area. The average SMB in zone 3 during AD 1400–2016 is 36 kg m^{-2} a^{-1}, with a std dev. of 38.7% for all transect regions. The average SMB in zone 4 is 29 kg m^{-2} a^{-1}, with a std dev. of only 12.3% and a minimum value of 19 kg m^{-2} a^{-1} across the zone. Zones 3 and 4 are located furthest from the coast and feature the highest elevations of the transect so little snow accumulation makes it from the coast; hence, the area is one of the lowest SMB in Antarctica (Ma and others, 2010).

5. Discussion

5.1. Undulating structures

Zone 3, which is located near Dome A, where the elevation changes dramatically and the surface is undulatory. The positive slope value indicates the uphill of the ice sheet surface along the direction of travel, so the average slope here is 1.97 m km^{-1},

ranging from −29.45 to 52.71 m km^{-1}. This zone is also the area with the largest SMB std dev. (Table 4), and undulating internal stratigraphy is visible (Fig. 5e). In the field, dunes were observed in the area more than 100 km from Dome A. Verfaillie and others (2012) also observed flat IRHs around Dome C, but the std dev. of IRHs depth increased in the area where the slope changed dramatically around Dome C. The appearance of this phenomenon is often related to katabatic winds and the slope of the ice sheet surface. Slope and wind-driven processes have a significant impact on snow redistribution, leading to an increase in the std dev. of the SMB (Arcone and others, 2005).

The SMB at spatial scales >20 km is affected by historical SMB and spatial patterns of surface processes (Frezzotti and others, 2007; Urbini and others, 2008). Zone 3 is a typical erosion-driven ablation area where the local slope is steep, and the area is affected by southwest winds (from right to left in Fig. 6). This area is dry year round, so topography and wind on the surface of the ice sheet are the main causes of erosion or irregular deposition (Table 5).

The surface slope and convexity/concavity are shown in Figure 6 to constrain the relationship between the SMB and the topography of the ice sheet surface. The convexity/concavity is calculated as the second derivative of the surface elevation and represents the curvature of the topography. Positive values indicate a concave surface aspect, where the terrain features local depressions/troughs, whereas negative values indicate a convex surface aspect, where the terrain features peaks (hills or dunes). Observing the peaks (gray shaded vertical lines) and troughs (blue shaded vertical lines) of the SMB in Figure 6, we find that the SMB is strongly related to surface convexity/concavity.

Calculating the average of the surface slope and convexity/concavity for each SMB maximum peak and minimum in zone 3 (Fig. 6b), we find that the average convexity/concavity at the SMB minima is −0.77 m km^{-2} and that the average slope is 4.24 m km^{-1}. These results indicate that the SMB minima typically occur leeward of large slopes and are associated with the divergence of wind fields and the erosion of snow caused by topographical peaks (Frezzotti and others, 2004; Ding and others, 2011). The average convexity/concavity of the SMB maxima is 3.85 m km^{-2} and the average slope is 2.32 m km^{-1}, indicating that SMB maxima tend to appear downwind of surface depressions with relatively low slopes. This is due to irregular deposition in snowdrifts and the convergence of the wind field in the terrain (van den Broeke and others, 2006).

Figure 6a shows the same analysis in the downstream part of zone 2, which has the second highest SMB std dev. Although the average slope in zone 2 shown in Figure 6a (1.89 m km^{-1}) is close to that in zone 3, the elevation rarely changes dramatically in the range of 10 km. An analysis of the surface topography at the positions of the maxima and minima of the SMB reveals that the average convexity/concavity at the SMB maxima is 2.30 m km^{-2}, and the average slope is close to zero. These results indicate that the SMB maxima tend to appear at the lowest elevation, i.e. in depressions. Although the average convexity/concavity at the SMB minima in zone 2 is positive, it is close to zero, similar to the average convexity/concavity at the SMB minima in zone 3. In addition, the average slope over the SMB minima in zone 3 is 1.59 m km^{-1}, further indicating that SMB minima typically occur at the inflection points of large slopes. Analyzing the relationships between SMB and surface topography of the ice sheet in zones 2 and 3 demonstrates that the SMB in these regions is most likely controlled by similar processes.

Although zone 1 has a steep slope and the highest annual average wind speed (Yang and others, 2007), it has a high SMB, which makes the surface of the ice sheet flat with no obvious dunes in
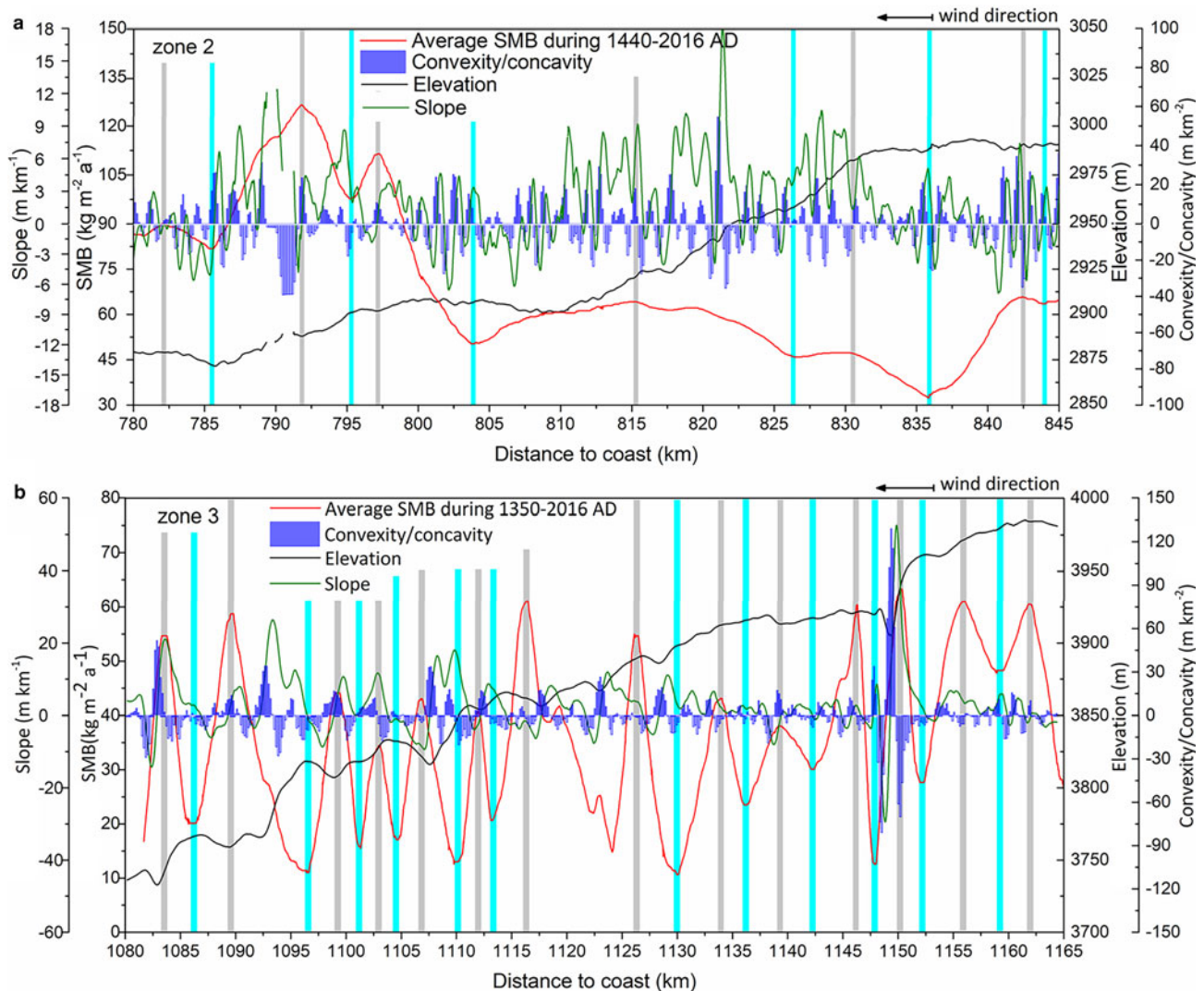
Fig. 6. Comparison of the average SMB (red) with the ice sheet surface elevation (black), slope (green), and convexity/concavity (blue) in (a) zone 2 and (b) zone 3. The convexity/concavity is smoothed by a window of 1.2 km. The gray shaded vertical lines represent SMB peaks, and the blue shaded vertical lines represent SMB troughs. The black arrow in the upper right corner indicates the wind direction. The blue dotted line represents the zero line for the slope and the convexity/concavity, which is used to highlight the trend of the terrain. Due to the failure of GPS sensors, elevation data near 790 km were briefly missing, as seen in (a).

Table 5. Average surface slopes and convexity/concavity for the SMB maxima and minima in zones 2 and 3

Zone	Convexity/concavity at peak m km^{-2}	Slope at peak m km^{-1}	Convexity/concavity at trough m km^{-2}	Slope at trough m km^{-1}
Zone 2	2.30	0.28	0.23	1.59
Zone 3	3.85	2.32	−0.77	4.24

local areas (<5 km; Ding and others, 2011); thus, the std dev. of the SMB is small (Xiao and others, 2005). However, zone 3 features one of the lowest SMB in East Antarctica, and continued snow erosion by strong katabatic winds causes substantial snow redistribution, which leads to large fluctuations in the SMB.

5.2. Spatial distribution in accumulation

Ignoring local-scale (<1 km) fluctuations, SMB decreases gradually with distance from the coast, which is consistent with previous results from this traverse route (Zhou and others, 2006; Ding and others, 2011; Li and others, 2012; Wang and others, 2012). In-depth comparison with multiple datasets (stake arrays, ice cores, regional atmospheric climate model (RACMO), and radar; Fig. 7) yields several observations:

(1) The SMB data from the stake observations (Fig. 7; light gray) were collected from AD 2009 to AD 2013 (recorded once a year) along the traverse, and the observations match the spatial variation features of our results. The SMB std dev. of our model in each region is one-half to one-third that of the stake measurements by Ding and others (2011), and zone 4 has the lowest SMB variability. This difference arises largely because our results are calculated over a longer period of time.

SMB in the RACMO is ~13 kg m^{-2} a^{-1} in the area around Dome A, which is lower than the value of 20 kg m^{-2} a^{-1} obtained by FMCW radar. This suggests that RACMO yields a systematic underestimation in low SMB regions, which is consistent with previous results (van de Berg and others, 2006).

(2) The ice core analysis method is performed by directly measuring the density, concentration of chemical ions and volcanic record to estimate SMB. According to Ding and others (2011), the coastal SMB rate during AD 1997–2008 gradually decreased, resulting in the radar measurement
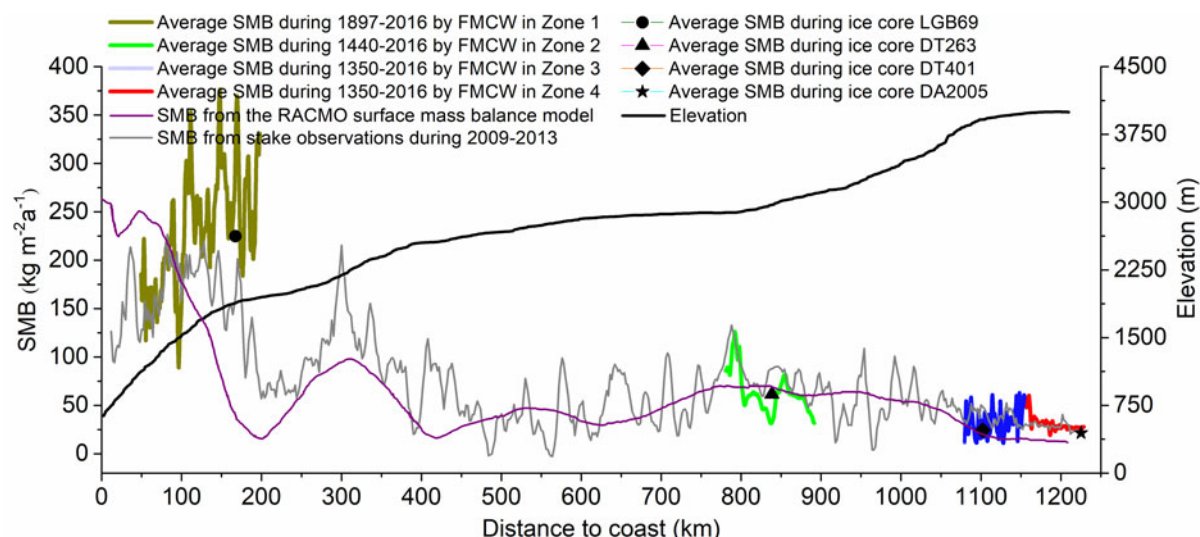
Fig. 7. Comparison of SMB estimates from different methods along the traverse route.

Table 6. Temporal variations in the average SMB at AD 1260–2016 for 18 km near ice core DT263

Zone	Distance to coast km	AD 1260–1343 MWP	AD 1343–1454	AD 1454–1836 LIA	AD 1836–1884	AD 1884–1904 Modern era	AD 1904–2016
Zone 2	806–824	85	71	36	59	127	145

Table 7. Temporal variations in the average SMB at AD 883–2016 for 30 km near ice core DA2005

Zone	Distance to coast km	AD 883–1062 MWP	AD 1062–1260	AD 1260–1388	AD 1388–1511	AD 1511–1644 LIA	AD 1644–2016 LIA and Modern era
Zone 4	1199–1229	22	20	31	35	35	27

result during AD 1928–2016 being lower than the result of the ice core LGB69 in AD 1928–2002. The radar SMB rates in this study are based on the ice core age–depth relationship, which is used to calibrate the ages of the IRHs in the radar data, and with Eqn (3); thus, our SMB rate results are not always the same as those based on ice core data, but there is a reasonable match between the radar and the ice core SMB results.

Müller and others (2010) investigated the East Antarctic plateau using 5.3 GHz (C-band) FMCW GPR and surveyed the ice divide near Dome A. They found that the SMB and its std dev. gradually increase around ice divided, which is in agreement with our observations.

5.3. Temporal variations in accumulation

Three IRHs were used to study the temporal variability in the SMB along the traverse over each time period. The periods of AD 1897–1918, AD 1918–1928 and AD 1928–2016 are shown for zone 1 in Table 4 and Figure 5. The SMB profiles between the three time periods are similar (with an average SMB of 235 kg m^{-2} a^{-1} over AD 1897–2016), indicating that the climate has been relatively stable over the past 100 years in this region (Tables 6 and 7).

The Medieval Warm Period (MWP; 10th–14th centuries) and the Little Ice Age (LIA; 15th–20th centuries) are the two most recent climate events (Stenni and others, 2002), which can help

understand the natural climate variability of Antarctica. Li and others (2009) speculated that LIA affected SMB only locally. The average SMB of zone 2 was 29 kg m^{-2} a^{-1} during AD 1440–1760, which is approximately one-third SMB of AD 1760–2016. SMB in zone 4 decreased by 20% between the 16th and 20th centuries (Table 4), but there was no significant change in the Dome A area. The limitation of IRH depth and the redistribution of snow may lead to distortion of IRH years (Frezzotti and others, 2002), so we only divide the transect region with less variable SMB near ice cores DT263 and DA2005 into six time periods for a more detailed temporal variation analysis (Tables 6 and 7).

During the MWP, the average SMB of zone 2 was 85 kg m^{-2} a^{-1} during AD 1260–1343 and decreased to 71 kg m^{-2} a^{-1} during AD 1343–1454. Furthermore, the average SMB was only 36 kg m^{-2} a^{-1} during AD 1454–1836. Then, it gradually increased through the 19th and 20th centuries to reach a modern SMB four times that of the LIA (145 kg m^{-2} a^{-1}). This temporal pattern of change is similar to that which occurred at Talos Dome (Stenni and others, 2002).

Since the average SMB of zone 4 is only 29 kg m^{-2} a^{-1}, the IRH depth after the 20th century is <10 m, which cannot be reliably identified in the radar-gram, so it is impossible to estimate the SMB temporal variations after the LIA. SMB increased from 22 to 35 kg m^{-2} a^{-1} during MWP and remained at 35 kg m^{-2} a^{-1} during AD 1511–1644, unlike zone 2. SMB in the Antarctic generally increased after the LIA (Bertler and others, 2011), but Dome A decreased to 27 kg m^{-2} a^{-1} during AD 1644–2016. SMB

at Dome A showed an opposite trend to zone 2 during LIA, which may be related to the different distribution of moisture origins (Stenni and others, 2002). Broecker and others (1999) pointed out that intense deep water formation may lead to the warming Antarctic during LIA.

To better understand the historical climate variability and its impact on SMB, it is necessary to expand spatial coverage of FMCW surveying in order to constrain time and space variability of SMB.

6. Conclusions

In the summer of 2015/16, a high-resolution FMCW radar was used to collect data along a 1236 km traverse from Zhongshan station to Dome A to examine the historical SMB record in this area for the first time. Through the analysis of the spatiotemporal variability in the internal radar stratigraphy, we demonstrated the following:

(1) The positions and depths of IRHs in the four distinct zones of the radar transect can be obtained from the radar-gram and the SMB variation characteristics can be obtained through calibration from ice core and stake data. The decreasing trend in the SMB with distance inland from the coast is evident in multiple datasets (stake arrays, ice cores, FMCW radar and RACMO).

(2) The shape of the IRHs is closely related to snowfall and surface snow redistribution. The decreasing trend in the SMB with distance inland from the coast is similar to that observed in Wilkes Land (Goodwin, 1991) and Dome Fuji (Fujita and others, 2011). SMB in zone 1 is high, which is due to the proximity to the coast and the steep slope, resulting in high precipitation rates. Although the slope is high, the surface elevation over small distances (<5 km) does not fluctuate considerably, so the resulting SMB spatial variability is low. Zone 2 has a flat topography, but the measured SMB fluctuates spatially due to the formation of wind-induced surface features such as wind crusts. The SMB during the LIA (AD 1454–1836) was only one-quarter of that during the 20th century. The topography in zone 3 is much rougher than for the other transect regions and features erosion-induced ablation surfaces. Snow erosion and accumulation occur in this area under the influence of katabatic wind interactions with the surface topography, inducing sharp fluctuations in the IRH geometries. In zone 4 (i.e. the Dome A area), the slope, snow precipitation and wind speeds are the lowest of the entire traverse, and the observed IRHs are the flattest and showed an opposite trend to zone 2 during LIA.

(3) The maximum SMB error is estimated to be $3.56 \, \mathrm{kg \, m^{-2} \, a^{-1}}$, and the most important factor is the error in the measured depth–density relationships. We obtain a strong correlation between modeled and observed densities at the ice core sites, with a maximum density error of $29 \, \mathrm{kg \, m^{-3}}$ obtained at ice core site DT263. This error may be due to the redistribution of snow causing anomalies in the densification process.

Radar measurements can provide SMB over a large area of the ice sheet and can be used to analyze the spatiotemporal variability in SMB. In most areas, SMB data are still severely lacking for temporal analysis. To understand the Antarctic response mechanism to climate events such as the MWP and LIA, it is necessary to conduct such a temporal analysis in East Antarctica with results that may help constrain the state of the ice sheet under climate warming.

References

Arcone S and Jacobel R (2010a) Effects of surface topography and wind on reflection horizons in ice sheets. In *Proceedings of the XIII International Conference on Ground Penetrating Radar*. IEEE, pp. 1–6. doi: 10.1109/ICGPR.2010.5550271.

Arcone S and Jacobel R (2010b) Unconformities, cosets, and folds within the East Antarctic ice sheet: 3.2 MHz profiles from a megadunes region of East Antarctica. In *2012 14th International Conference on Ground Penetrating Radar (GPR)*. IEEE, pp. 718–723.

Arcone SA, Spikes VB and Hamilton GS (2005) Stratigraphic variation within polar firn caused by differential accumulation and ice flow: interpretation of a 400 MHz short-pulse radar profile from West Antarctica. *Journal of Glaciology* **51**(174), 407–422.

Arcone SA and Yankielun NE (2000) 1.4 GHz Radar penetration and evidence of drainage structures in temperate ice: Black Rapids Glacier, Alaska, USA. *Journal of Glaciology* **46**(154), 477–490.

Bertler NAN, Mayewski PA and Carter L (2011) Cold conditions in Antarctica during the little Ice Age—implications for abrupt climate change mechanisms. *Earth and Planetary Science Letters* **308**(1–2), 41–51.

Broecker WS, Sutherland S and Peng TH (1999) A possible 20th-century slowdown of Southern Ocean deep water formation. *Science (New York, N.Y.)* **286**(5442), 1132–1135.

Cuffey KM and Paterson WSB (2010) *The Physics of Glaciers*, 4th edn. Butterworth-Heinemann, Oxford.

Cui X and 7 others (2010) Ice radar investigation at Dome A, East Antarctica: ice thickness and subglacial topography. *Chinese Science Bulletin* **55**(4–5), 425–431.

Cui X, Wang T, Sun B, Tang X and Guo J (2017) Chinese Radio glaciological studies on the Antarctic ice sheet: progress and prospects. *Advances in Polar Science* **28**, 161–170.

Dahl-Jensen D and 131 others (2013) Eemian interglacial reconstructed from a Greenland folded ice core. *Nature* **493**(7433), 489–494.

Delmas RJ, Kirchner S, Palais JM and Petit JR (1992) 1000 Years of explosive volcanism recorded at South Pole. *Tellus Series B* **44**, 335–350.

Ding M and 6 others (2011) Spatial variability of surface mass balance along a traverse route from Zhongshan station to Dome A, Antarctica. *Journal of Glaciology* **57**(204), 658–666.

Eisen O and 15 others (2008) Ground-based measurements of spatial and temporal variability of snow accumulation in East Antarctica. *Reviews of Geophysics* **46**(RG2), RG2001.

Ellerbruch DA and Boyne HS (1980) Snow stratigraphy and water equivalence measured with an active microwave system. *Journal of Glaciology* **26** (94), 225–233.

Frezzotti M and 13 others (2004) New estimations of precipitation and surface sublimation in East Antarctica from snow accumulation measurements. *Climate Dynamics* **23**(7–8), 803–813.

Frezzotti M and 13 others (2005) Spatial and temporal variability of snow accumulation in East Antarctica from traverse data. *Journal of Glaciology* **51**(172), 113–124.

Frezzotti M, Gandolfi S and Urbini S (2002) Snow megadunes in Antarctica: sedimentary structure and genesis. *Journal of Geophysical Research* **107** (D18), 4344.

Frezzotti M, Urbini S, Proposito M, Scarchilli C and Gandolfi S (2007) Spatial and temporal variability of surface mass balance near Talos Dome, East Antarctica. *Journal of Geophysical Research* **112**(F02), 032. doi: 10.1029/2006JF000638.

Fujita S and 25 others (2011) Spatial and temporal variability of snow accumulation rate on the East Antarctic ice divide between Dome Fuji and EPICA DML. *The Cryosphere* **5**(4), 1057–1081.

Goodwin ID (1991) Snow-accumulation variability from seasonal surface observations and firn-core stratigraphy, eastern Wilkes Land, Antarctica. *Journal of Glaciology* **37**(127), 383–387.

Gubler H and Hiller M (1984) The use of microwave FMCW radar in snow and avalanche research. *Cold Regions Science and Technology* **9**(2), 109–119.

Herron MM and Langway CC (1980) Firn densification: an empirical model. *Journal of Glaciology* **25**(93), 373–385.

Hou S, Li Y, Xiao C and Ren J (2007) Recent accumulation rate at Dome A, Antarctica. *Chinese Science Bulletin* **52**(3), 428–431.

Jacobel RW and Hodge SM (1995) Radar internal layers from the Greenland summit. *Geophysical Research Letters* **22**(5), 587–590.

Jiang S and 7 others (2012) A detailed 2840 year record of explosive volcanism in a shallow ice core from Dome A, East Antarctica. *Journal of Glaciology* **58**(207), 65–75.

Kameda T, Motoyama H, Fujita S and Takahashi S (2008) Temporal and spatial variability of surface mass balance at Dome Fuji, East Antarctica, by the stake method from 1995 to 2006. *Journal of Glaciology* **54**(184), 107–116.

Kanagaratnam P, Gogineni SP, Gundestrup N and Larsen L (2001) High-resolution radar mapping of internal layers at the North Greenland Ice Core Project. *Journal of Geophysical Research: Atmospheres* **106**(D24), 33799–33811.

Koh G, Lever JH, Arcone SA, Marshall HP and Ray LE (2010) Autonomous FMCW radar survey of Antarctic shear zone. *Proceedings of the XIII International Conference on Ground Penetrating Radar*, Lecce, Italy, 1–5. doi: 10.1109/ICGPR.2010.5550174.

Koh G, Yankielun NE and Baptista AI (1996) Snow cover characterization using multiband FMCW radars. *Hydrological Processes* **10**(12), 1609–1617.

Kovacs A, Holladay JS and Bergeron CJ (1995) The footprint/altitude ratio for helicopter electromagnetic sounding of sea-ice thickness: comparison of theoretical and field estimates. *Geophysics* **60**(2), 374–380.

Lavigne F and 14 others (2013) Source of the great A.D. 1257 mystery eruption unveiled, Samalas volcano, Rinjani Volcanic Complex, Indonesia. *Proceedings of the National Academy of Sciences of the United States of America* **110**(42), 16742–16747.

Lenaerts JT, Medley B, van den Broeke MR and Wouters B (2019) Observing and modeling ice sheet surface mass balance. *Reviews of Geophysics* **57**(2), 376–420.

Li Y, Cole-Dai J and Zhou L (2009) Glaciochemical evidence in an east Antarctica ice core of a recent (AD 1450–1850) neoglacial episode. *Journal of Geophysical Research* **114**(D08), 117. doi: 10.1029/2008jd011091.

Li RX, Xiao CD, Sneed SB and Yan M (2012) A continuous 293-year record of volcanic events in an ice core from Lambert Glacier basin, East Antarctica. *Antarctic Science* **24**(3), 293–298.

Looyenga H (1965) Dielectric constants of heterogeneous mixtures. *Physica* **31** (3), 401–406.

Ma Y, Bian L, Xiao C, Allison I and Zhou X (2010) Near surface climate of the traverse route from Zhongshan Station to Dome A, East Antarctica. *Antarctic Science* **22**(4), 443–459.

Marshall H and Koh G (2008) FMCW Radars for snow research. *Cold Regions Science and Technology* **52**(2), 118–131.

Marshall HP, Schneebeli M and Koh G (2007) Snow stratigraphy measurements with high-frequency FMCW radar: comparison with snow micro-penetrometer. *Cold Regions Science and Technology* **47**(1), 108–117.

Mayewski PA and 18 others (2005) The international trans-Antarctic scientific expedition (ITASE): an overview. *Annals of Glaciology* **41**(1), 180–185.

Meur EL and 7 others (2018) Spatial and temporal distributions of surface mass balance between Concordia and Vostok stations, Antarctica, from combined radar and ice core data: first results and detailed error analysis. *The Cryosphere* **12**(5), 1831–1850.

Moore JC, Narita H and Maeno N (1991) A continuous 770-year record of volcanic activity from East Antarctica. *Journal of Geophysical Research* **96** (9), 17353–17359.

Müller K and 6 others (2010) An 860 km surface mass-balance profile on the East Antarctic plateau derived by GPR. *Annals of Glaciology* **51**(55), 1–8.

Proksch M, Löwe H and Schneebeli M (2015) Density, specific surface area, and correlation length of snow measured by high-resolution penetrometry. *Journal of Geophysical Research: Earth Surface* **120**, 346–362.

Qin D and 8 others (2000) Primary results of glaciological studies along an 1100 km transect from Zhongshan station to Dome A, East Antarctic ice sheet. *Annals of Glaciology* **31**(1), 198–204.

Ren J and 6 others (2010) A 2680 year volcanic record from the DT401 East Antarctic ice core. *Journal of Geophysical Research* **115**, D11301.

Ren J, Qin D and Xiao C (2001) Preliminary results of the inland expeditions along a transect from the Zhongshan Station to Dome A, East Antarctica. *Journal of Glaciology and Geocryology* **23**(1), 51–56.

Rignot E, Velicogna I, van den Broeke MR, Monaghan A and Lenaerts JTM (2011) Acceleration of the contribution of the Greenland and Antarctic ice sheets to sea level rise. *Geophysical Research Letters* **38**(5), L05503.

Shepherd A and 46 others (2012) A reconciled estimate of ice-sheet mass balance. *Science (New York, N.Y.)* **338**(6111), 1183–1189.

Solomon S and 7 others (2007) Climate change 2007: the physical science basis. Contribution of working group i to the fourth assessment report of the intergovernmental panel on climate change. *Intergovernmental Panel on Climate Change Climate Change* **18**(2), 95–123.

Stenni B and 6 others (2002). Eight centuries of volcanic signal and climate change at Talos Dome (East Antarctica). *Journal of Geophysical Research: Atmospheres* **107**(D9), 4076. doi: 10.1029/2000JD000317.

Tang X, Sun B, Li Y, Cui X and Li X (2009) Some recent progress of Antarctic ice sheet research. *Advances in Earth Science* **24**(11), 1210–1218.

Urbini S and 6 others (2008) Historical behaviour of Dome C and Talos Dome (East Antarctica) as investigated by snow accumulation and ice velocity measurements. *Global Planet Change* **60**(3), 576–588.

Uribe J, Zamora R, Gacitúa G, Rivera A and Ulloa D (2014) A low power consumption radar system for measuring ice thickness and snow/firn accumulation in Antarctica. *Annals of Glaciology* **55**(67), 39–48.

van de Berg WJ, van den Broeke MR, Reijmer CH and van Meijgaard E (2006) Reassessment of the Antarctic surface mass balance using calibrated output of a regional atmospheric climate model. *Journal of Geophysical Research: Atmospheres* **111**(D11), 104. doi: 10.1029/2005JD006495.

van den Broeke MR, De Berg WJ, van Meijgaard E and Reijmer CH (2006) Identification of Antarctic ablation areas using a regional atmospheric climate model. *Journal of Geophysical Research* **111**, 1–14.

Verfaillie D and 7 others (2012) Snow accumulation variability derived from radar and firn core data along a 600 km transect in Adelie Land, East Antarctic plateau. *The Cryosphere* **6**, 1345–1358.

Waddington ED, Neumann TA, Koutnik MR, Marshall H-P and Morse DL (2007) Inference of accumulation-rate patterns from deep layers in glaciers and ice sheets. *Journal of Glaciology* **53** (183), 694–712.

Wang Y, Sodemann H, Shugui H, Masson-Delmotte V, Jouzel J and Pang H (2012) Snow accumulation and its moisture origin over Dome Argus, Antarctica. *Climate Dynamics* **40**(3–4), 731–742.

Xiao C, Qin D, Bian L, Zhou X, Allison I and Yan M (2005) A precise monitoring of snow surface height in the region of Lambert Glacier basin-Amery Ice Shelf, East Antarctica. *Science in China Series D: Earth Sciences* **48**(1), 100–111.

Yamaguchi Y, Mitsumoto M, Sengoku M and Abe T (1992) Human body detection in wet snowpack by an FM-CW radar. *IEEE Transactions on Geoscience and Remote Sensing* **30**(1), 186–189.

Yang W, Dou Y, Lang S, Guo J, Pan Y and Chen Y (2019) Distribution of shallow isochronous layers in East Antarctica inferred from frequency-modulated continuous-wave (FMCW) radar. *Annals of Geophysics* **62**, 24.

Yang Q, Yin T, Zhang L and Jiang D (2007) Analyses of surface winds along the track from Zhongshan Station to Dome A, Antarctica. *Chinese Journal of Polar Research* **19**(4), 295–304.

Yankielun N, Rosenthal W and Davis RE (2004) Alpine snow depth measurements from aerial FMCW radar. *Cold Regions Science and Technology* **40**(1), 123–134.

Zhou L and 7 others (2006) A 780-year record of explosive volcanism from DT263 ice core in east Antarctica. *Chinese Science Bulletin* **51**(22), 2771–2780.

Appendix A: converting TWT to depth

The transmitting antenna produces an electromagnetic wave and part of the wave is reflected when passing through a layer within the ice sheet. These reflected signals are received by the receiving antenna and are compared with the reference signal generated by the voltage-controlled oscillator to calculate the TWT of the electromagnetic wave based on the frequency difference. To convert TWT to depths in ice, TWT is divided by the speed of electromagnetic waves in ice (e.g. Yang and others, 2019).

However, to assign ice core ages to the interpreted IRHs, real depths must be assigned to the IRHs. The firn/ice column, especially in the first 100 m, is a layered media composed of a mixture of air and firn (Kanagaratnam and others, 2001). As the depth increases, the air content in the firn continuously decreases. This densification process causes the density and crystal structure of the firn/ice to change. The permittivity is mainly influenced by density (Verfaillie and others, 2012). As shown in Eqn (A1), this process affects the electromagnetic wave velocity. However, the electromagnetic wave velocity is needed to convert the TWT to depth. The electromagnetic wave propagation in a given medium is described as follows:

$$c = \frac{c_v}{\sqrt{\varepsilon}} \tag{A1}$$

where c_v is the wave velocity in a vacuum (i.e. 0.3 m ns^{-1}) and the wave velocity c in the medium (firn/ice) is directly affected by the permittivity ε.

The density of ice increases with depth and the rate of this change gradually slows after exceeding a critical density (830 kg m^{-3}) (Ren and others, 2001). Assuming that there are no jumps in the density change trend, the Looyenga (1965) model is used to calculate the dielectric permittivity of such layered media according to

$$\varepsilon = [(\varepsilon_2^{1/3} - \varepsilon_1^{1/3})v + \varepsilon_1^{1/3}]^3 \tag{A2}$$

where ε_2 is the dielectric constant of ice (i.e. 3.15; Kanagaratnam and others, 2001), ε_1 is the dielectric constant of air (i.e. 1), and v is the volume fraction of ice in the firn obtained by the following equation:

$$v = \frac{\rho}{\rho_i} \tag{A3}$$

where ρ is the density of the firn and ρ_i is the density of pure ice (i.e. 918 kg m^{-3}; Kanagaratnam and others, 2001).

Finally, by introducing Eqns (A1) and (A3) into Eqn (A2), we obtain the following expression:

$$c = c_v \times \left[(\varepsilon_2^{1/3} - \varepsilon_1^{1/3}) \frac{\rho}{\rho_i} + \varepsilon_1^{1/3} \right]^{-3/2} \tag{A4}$$

Using Eqn (A4), the change in electromagnetic wave velocity over the vertical profile is calculated using the density–depth relationship measured in the field (see Section 2.2).